THE FINITE-DIFFERENCE TIME-DOMAIN METHOD FOR NUMERICAL MODELING OF ELECTROMAGNETIC WAVE INTERACTIONS

Allen Taflove, *Department of Electrical Engineering and Computer Science, McCormick School of Engineering, Northwestern University, Evanston, Illinois 60208, USA*

Korada R. Umashankar, *Department of Electrical Engineering and Computer Science, University of Illinois at Chicago, Chicago, Illinois 60680, USA*

ABSTRACT

This paper succinctly reviews the background and formulation of the finite-difference time-domain (FD-TD) method for numerical modeling of electromagnetic wave interactions with arbitrary structures. Selected 3-D results are given showing comparisons with both measured data and other numerical modeling approaches. An assessment is made of the present horizon of FD-TD modeling capabilities, and possible future directions.

1. INTRODUCTION

Accurate numerical modeling of full-vector electromagnetic (EM) wave interactions with arbitrary structures is difficult. Typical structures of engineering interest have shapes, apertures, cavities, and material compositions that produce near fields that cannot be resolved into finite sets of modes or rays. Proper numerical modeling of such near fields requires sampling at sub-wavelength (sub-λ) resolution to avoid aliasing of magnitude and phase information. The goal is to provide a self-consistent model of the mutual coupling of the electrically-small cells comprising the structure, even if the structure spans tens of λ in 3-D.

This paper reviews the formulation and applications of a candidate numerical modeling approach for this purpose: the finite-difference time-domain (FD-TD) solution of Maxwell's curl equations. FD-TD is very simple in concept and execution. However, it is remarkably robust, providing highly accurate modeling predictions for a wide variety of EM wave interaction problems. FD-TD is analogous to existing finite-difference solutions of scalar wave propagation and fluid flow problems in that the numerical model is based upon a direct, time-domain solution of the governing partial differential equation. Yet, FD-TD is a nontraditional approach to numerical electromagnetics for engineering applications where frequency-domain integral equation approaches have dominated for 25 years.

One of the goals of this paper is to demonstrate that recent advances in FD-TD modeling concepts and software implementation, combined with advances in computers, have expanded the scope, accuracy, and speed of FD-TD modeling to the point where it may be the best choice for large EM wave interaction problems. With this in mind, this paper will succinctly review selected 2-D and 3-D FD-TD modeling validations and examples:

1. EM wave penetration and coupling
   a. Narrow slot in a thick screen (2-D, TE-polarized case)
   b. Wires in free space and in a metal cavity (2-D and 3-D)

Electromagnetics 10:105–126, 1990

2. Scattering and radar cross section (RCS)
   a. T-shaped conducting target, multiple monostatic looks (3-D)
   b. Trihedral corner reflector, both bare metal and with absorbing coating (3-D)
   c. Wing-like structure, conformally modeled (2-D, TM-polarized case)
   d. Jet engine inlet, conformally modeled (3-D)

Finally, this paper will conclude with an assessment of the present horizon of FD-TD modeling capabilities, and possible future directions.

2. GENERAL CHARACTERISTICS OF FD-TD

FD-TD is a direct solution of Maxwell's time-dependent curl equations. It employs no potentials. Instead, it applies simple, second-order accurate central-difference approximations [1] for the space and time derivatives of the electric (E) and magnetic (H) fields directly to the differential operators of the curl equations. This achieves a sampled-data reduction of the continuous EM field in a volume of space over a period of time. Space and time discretizations are selected to bound errors in the sampling process and to insure numerical stability of the algorithm [2]. Overall, FD-TD is a marching-in-time procedure which simulates the continuous actual waves by sampled-data numerical analogs propagating in a computer data space. The system of equations to update E and H is fully explicit, so that there is no need to solve simultaneous equations. Thus, the required computer storage and running time is dimensionally low, proportional only to N, where N is the number of EM field unknowns in the volume modeled.

Fig. 1a illustrates the time-domain wave tracking concept of the FD-TD method. A region of space having initially zero fields is selected for field sampling in space and time. At t=0, it is assumed that an incident plane wave enters the region. Propagation of this wave is modeled by time-stepping, i.e., simply implementing the finite-difference analog of the curl equations. Time-stepping continues as the numerical analog of the incident wave strikes the modeled target embedded within the sampling region. All outgoing scattered wave analogs ideally propagate through the lattice truncation planes with negligible reflection to exit the region. Phenomena such as induction of surface currents, scattering

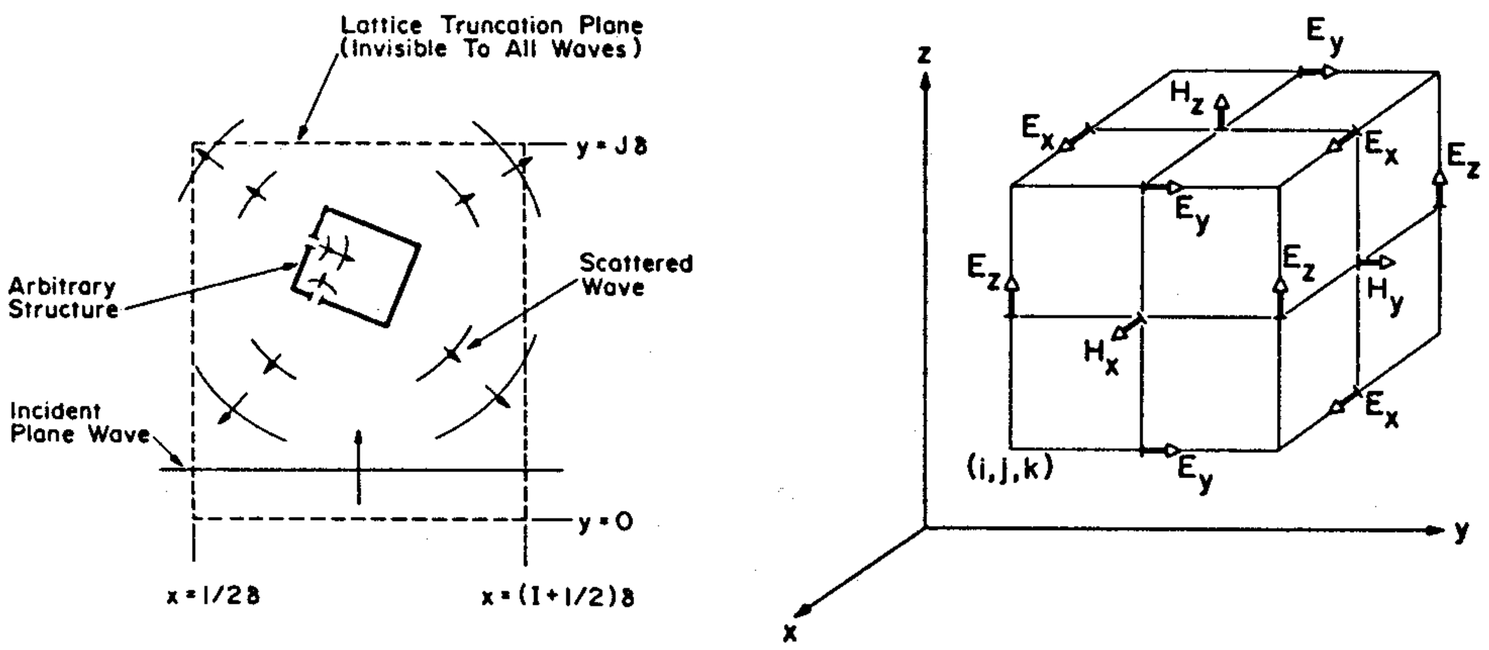

Fig. 1. Basic elements of the FD-TD space lattice.
(a) Time-domain wave tracking concept; (b) Lattice unit cell in Cartesian coordinates.

and multiple scattering, aperture penetration, and cavity excitation are modeled time-step by time-step by the action of the curl equations analog. Self-consistency of these modeled phenomena is generally assured if their spatial and temporal variations are well resolved by the space and time sampling process.

Time-stepping is continued until the desired late-time pulse response or steady-state behavior is observed. An important example of the latter is the sinusoidal steady state, wherein the incident wave is assumed to have a sinusoidal dependence, and time-stepping is continued until all fields in the sampling region exhibit sinusoidal repetition. This is a consequence of the limiting amplitude principle [3]. Extensive numerical experimentation with FD-TD has shown that the number of complete cycles of the incident wave required to be time-stepped to achieve the sinusoidal steady state is a function of two (possibly related) factors:

1) *Target electrical size.* Numerical wave analogs must be permitted time to propagate in the FD-TD grid to causally connect the physics of all regions of the target. For many targets, this requires a number of time steps sufficient to permit at least two front-to-back-to-front traverses of the target by a wave analog. For example, assuming a target spanning10λ, at least 40 cycles of the incident wave should be time-stepped to approach the sinusoidal steady state. For a grid resolution of $\lambda/10$, this corresponds to 800 time steps.

2) *Target Q factor.* Targets having well-defined low-loss cavities or low-loss dielectric compositions may require the number of complete cycles of the incident wave to be time-stepped to approach the Q factor of the resonance. Because Q can be large even for electrically moderate size cavities, this can dictate how many time steps the FD-TD code must be run.

In the RCS area, target electrical size may often be the dominant factor. Cavities for RCS problems (such as engine inlets) tend to be open, and therefore moderate Q; and the use of radar-absorbing material (RAM) serves further to reduce the Q factors of structures.

Fig. 1b illustrates the positions of the E and H vector components about a unit cell of the FD-TD lattice in Cartesian coordinates [1]. Note that each H component is surrounded by four circulating E components, and vice versa. This arrangement permits not only a centered-difference analog to the space derivatives of the curl equations, but also a natural geometry for implementing the integral form of Faraday's Law and Ampere's Law at the space-cell level. This integral interpretation permits a simple but effective modeling of the physics of thin-slot coupling, thin-wire coupling, and smoothly curved target surfaces, as will be seen in Section 4.

An arbitrary 3-D scatterer can be embedded in an FD-TD lattice simply by assigning desired values of electrical permittivity and conductivity are to each lattice E component, and magnetic permeability and equivalent loss to each H component. These are interpreted by the FD-TD program as local coefficients for the time-stepping algorithm. Specification of media properties in this component-by-component manner results in a staircase approximation of curved surfaces, and assures continuity of tangential fields at the interface of dissimilar media with no need for special field matching. In the 1970's through mid-1980's, the staircase approximation of curved surfaces was found to be adequate in FD-TD modeling problems involving EM wave interactions with biological tissues [4],[5], penetration into cavities [6]-[8], and pulse interactions with structures [9]-[11]. However, recent interest in wide dynamic range models of scattering has prompted the development of *fully surface-conforming* FD-TD approaches. One such approach is summarized in Section 4c.

3. BASIC FD-TD ALGORITHM DETAILS

a. Time-Stepping Algorithm

Table 1 lists the six coupled equations for E and H that comprise Maxwell's equations in Cartesian coordinates, and the central-difference approximations to the space and time partial derivatives of these equations, using a sampled-field notation.

$$\frac{\partial H_x}{\partial t} = \frac{1}{\mu}\left(\frac{\partial E_y}{\partial z} - \frac{\partial E_z}{\partial y} - \rho' H_x\right)$$
$$\frac{\partial H_y}{\partial t} = \frac{1}{\mu}\left(\frac{\partial E_z}{\partial x} - \frac{\partial E_x}{\partial z} - \rho' H_y\right)$$
$$\frac{\partial H_z}{\partial t} = \frac{1}{\mu}\left(\frac{\partial E_x}{\partial y} - \frac{\partial E_y}{\partial x} - \rho' H_z\right)$$
$$\frac{\partial E_x}{\partial t} = \frac{1}{\epsilon}\left(\frac{\partial H_z}{\partial y} - \frac{\partial H_y}{\partial z} - \sigma E_x\right)$$
$$\frac{\partial E_y}{\partial t} = \frac{1}{\epsilon}\left(\frac{\partial H_x}{\partial z} - \frac{\partial H_z}{\partial x} - \sigma E_y\right)$$
$$\frac{\partial E_z}{\partial t} = \frac{1}{\epsilon}\left(\frac{\partial H_y}{\partial x} - \frac{\partial H_x}{\partial y} - \sigma E_z\right)$$

where:

E_x, E_y, E_z = Cartesian components of electric field, volts/meter

H_x, H_y, H_z = Cartesian components of magnetic field, volts/meter

ϵ = electric permittivity, farads/meter

σ = electric conductivity, siemens/meter

μ = magnetic permeability, henrys/meter

ρ' = equivalent magnetic loss, ohms/meter

$$(i,j,k) = (i\Delta x, j\Delta y, k\Delta z)$$
$$F^n(i,j,k) = F(i\Delta x, j\Delta y, k\Delta z, n\Delta t)$$
$$\frac{\partial F^n(i,j,k)}{\partial x} = \frac{F^n(i+\frac{1}{2},j,k) - F^n(i-\frac{1}{2},j,k)}{\Delta x} + \text{order}(\Delta x^2)$$
$$\frac{\partial F^n(i,j,k)}{\partial t} = \frac{F^{n+\frac{1}{2}}(i,j,k) - F^{n-\frac{1}{2}}(i,j,k)}{\Delta t} + \text{order}(\Delta t^2)$$

For a cubic space lattice, $\Delta x = \Delta y = \Delta z \equiv \delta$

Table 1. Maxwell's equations and central-difference approximations.

Upon substituting the central-difference approximations for the space and time derivatives into Maxwell's equations, six coupled finite-difference time-stepping expressions arise for the Cartesian components of E and H. These expressions permit a progressive time integration of the Maxwell's equations suitable for the solution of an initial-value problem. The following is a sample time-stepping expression for an electric field component:

$$E_z^{n+1}(i,j,k+1/2) = \frac{1-\frac{\sigma(i,j,k+1/2)\Delta t}{2\epsilon(i,j,k+1/2)}}{1+\frac{\sigma(i,j,k+1/2)\Delta t}{2\epsilon(i,j,k+1/2)}} E_z^n(i,j,k+1/2) + \frac{1}{1+\frac{\sigma(i,j,k+1/2)\Delta t}{2\epsilon(i,j,k+1/2)}} \times$$

$$\frac{\Delta t}{\epsilon(i,j,k+1/2)} \left[\begin{array}{l} \frac{1}{\Delta x}\left(H_y^{n+\frac{1}{2}}(i+\frac{1}{2},j,k+\frac{1}{2}) - H_y^{n+\frac{1}{2}}(i-\frac{1}{2},j,k+\frac{1}{2})\right) + \\ \\ \frac{1}{\Delta y}\left(H_x^{n+\frac{1}{2}}(i,j-\frac{1}{2},k+\frac{1}{2}) - H_x^{n+\frac{1}{2}}(i,j+\frac{1}{2},k+\frac{1}{2})\right) \end{array} \right] \qquad (1)$$

Time-stepping expressions for the other electric field components follow by analogy. For the magnetic field components, the magnetic permeability μ and equivalent loss ρ' simply appear in place of the electric permittivity ϵ and conductivity σ.

The time-stepping system represented by (1) is fully explicit. That is, the new value of a field vector component at any lattice point depends only on its previous value and on previous values of the other field. Therefore, at any given time step, the updating of a field vector can proceed one point at a time; or, if *p* parallel processors are employed concurrently, *p* points at a time.

To insure the stability of the time-stepping algorithm exemplified by (1), Δt is chosen to satisfy the inequality [2],[8]

$$\Delta t \leq \frac{1}{c_{max}\left\{\frac{1}{\Delta x^2}+\frac{1}{\Delta y^2}+\frac{1}{\Delta z^2}\right\}^{\frac{1}{2}}} \qquad (2)$$

where c_{max} is the maximum EM wave phase velocity within the media being modeled. Note that the corresponding stability criterion in [1, Eqns. (7) and (8)] is incorrect [2],[8].

b. Numerical Dispersion

The numerical algorithm for Maxwell's curl equations represented by (1) causes dispersion of the simulated wave modes in the computational lattice. That is, the phase velocity of numerical modes in the FD-TD lattice can vary with modal wavelength, direction of propagation, and lattice discretization. Since numerical dispersion can lead to non-physical results such as pulse distortion, anisotropy, and refraction, it is a factor in FD-TD modeling that must be accounted to understand the operation of the algorithm and its accuracy limits.

Following the analysis in [8], it can be shown that the numerical dispersion relation for the 3-D case represented by (1) is given by

$$\left(\frac{1}{c\Delta t}\right)^2 \sin^2\left(\frac{\omega\Delta t}{2}\right) = \frac{1}{\Delta x^2}\sin^2\left(\frac{k_x\Delta x}{2}\right) + \frac{1}{\Delta y^2}\sin^2\left(\frac{k_y\Delta y}{2}\right) + \frac{1}{\Delta z^2}\sin^2\left(\frac{k_z\Delta z}{2}\right) \tag{3}$$

where k_x, k_y, and k_z are, respectively, the x, y, and z components of the wavevector; ω is the wave angular frequency; and c is the speed of light in the homogeneous material being modeled.

In contrast to the numerical dispersion relation, the analytical dispersion relation for a plane wave in a continuous, lossless medium is just

$$\omega^2/c^2 = k_x^2 + k_y^2 + k_z^2 \tag{4}$$

for the 3-D case. We can easily show that (3) reduces to (4) in the limit as Δt, Δx, Δy,and Δz all go to zero. Qualitatively, this suggests that numerical dispersion can be reduced to any degree that is desired if we only use a fine-enough FD-TD gridding.

To quantitatively illustrate the dependence of numerical dispersion upon FD-TD grid discretization, we shall take as an example the 2-D case ($\Delta z = \infty$), assuming for simplicity square unit cells. Fig. 2 provides results for this case showing the variation of numerical wave phase velocity with wave propagation angle in the grid [8].

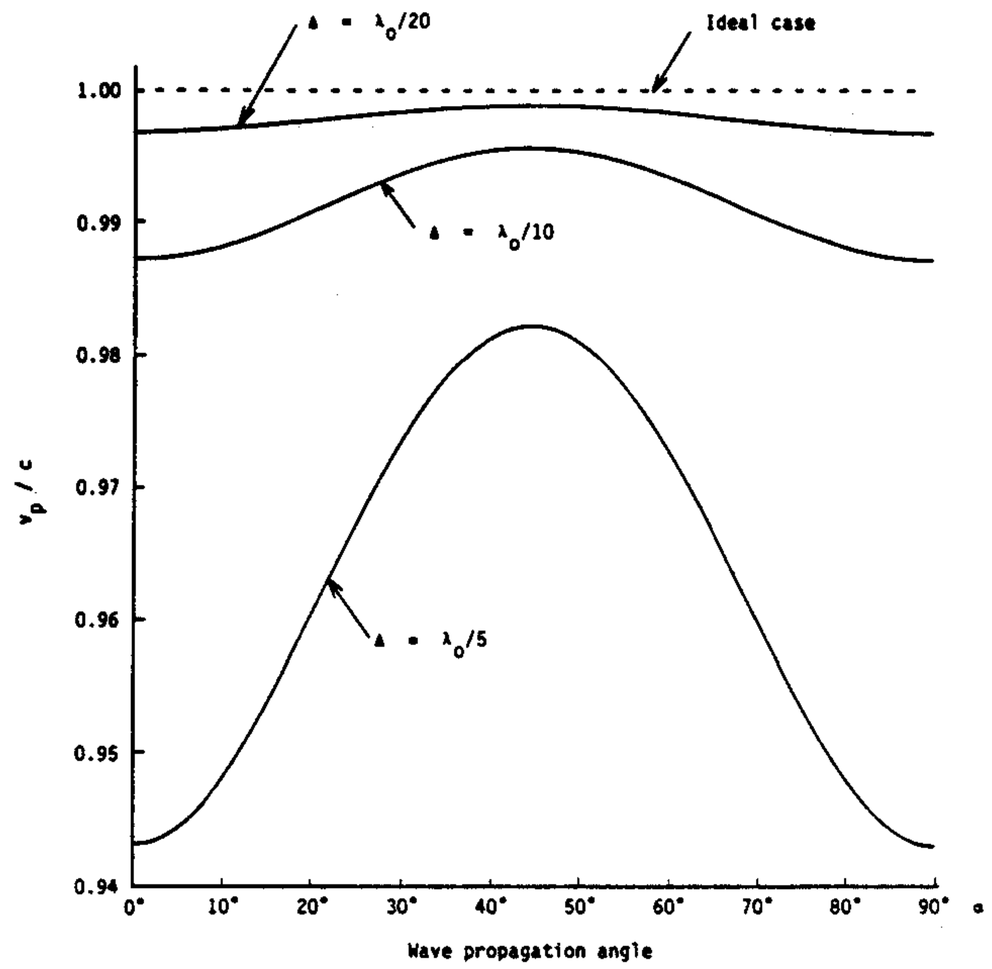

Fig. 2. Variation of FD-TD numerical wave phase velocity with wave propagation angle in the grid for three different grid discretizations.

In Fig. 2, three different grid resolutions of the propagating wave are examined: $\lambda/5$; $\lambda/10$; and $\lambda/20$. For each resolution, the relation $c\Delta t = \delta/2$ is maintained. This relation is commonly used in 2-D and 3-D FD-TD codes to satisfy the numerical stability criterion of (2) with ample safety margin. It is seen that the numerical phase velocity is maximum at 45^o (oblique incidence), and minimum at 0^o and 90^o (incidence along either Cartesian grid axis) for all grid resolutions. This represents a numerical anisotropy that is inherent in the Yee algorithm. However, the velocity error diminishes quadratically with grid resolution, so that the worst-case velocity error is -1.3% for $\lambda/10$ grid resolution, but only -0.31% for $\lambda/20$ resolution.

In addition to numerical phase velocity anisotropy and pulse distortion effects, numerical dispersion could lead to non-physical refraction of propagating modes if the cell size is a function of position in the grid. This is because the modal phase velocity distribution would vary with position in the grid, just as in an inhomogeneous medium. The error level would depend upon the magnitude and abruptness of the changes of the phase velocity distribution, and could be estimated by using conventional theory for wave refraction at dielectric interfaces.

c. Lattice Zoning and Plane Wave Source Condition

The numerical algorithm for Maxwell's curl equations defined by the finite-difference system reviewed above has a linear dependence upon the components of the EM field vectors. Therefore, this system can be applied with equal validity to either the incident-field, the scattered-field, or the total-field vector components. Present FD-TD codes utilize this property to divide the numerical lattice into two distinct zones, a total-field zone and a scattered-field zone, as shown in Fig. 3a. These zones are separated by a

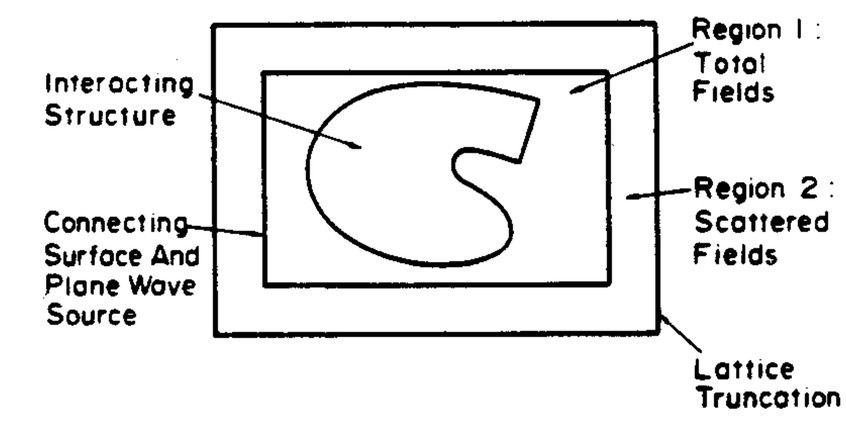

Fig. 3. Zoning of the FD-TD lattice. (a) Total-field and scattered-field regions; (b) Near-to-far field integration surface located in the scattered-field region.

rectangular virtual surface which serves to connect the fields in each region [12],[13]. The interacting structure of interest is embedded within the total-field zone.

The total-field/scattered-field lattice zoning shown in Fig. 3a provides a number of key features which enhance the computational flexibility and dynamic range of the FD-TD method:

1) *Arbitrary incident wave.* The connecting condition provided at the interface of the inner and outer regions, which assures consistency of the numerical space derivative operations across the interface, simultaneously generates an arbitrary incident plane wave in Region 1 having a user-specified time waveform, angle of incidence, and angle of polarization. This connecting condition, discussed in [8], almost completely confines the incident wave to Region 1 and yet is transparent to outgoing scattered wave modes which are free to enter Region 2.

2) *Simple programming of inhomogeneous structures.* Embedding the modeled structure in the total-field region permits a natural satisfaction of tangential field continuity across media interfaces without having to compute the incident field at possibly tens of thousands of points along complicated media-interface loci that are unique to each structure. The zoning arrangement of Fig. 3a requires computation of the incident field only along the rectangular connecting surface between total-field and scattered-field regions. This surface is fixed, i.e., independent of the shape or composition of the enclosed modeled structure. A substantial benefit in computer running time arises as a result, one that increases as the complexity of the target increases.

3) *Large near-field computational dynamic range.* Because the modeled structure is embedded in the total-field region, low total-field levels in shadow regions or within shielding enclosures are computed directly without suffering subtraction noise (as would be the case if scattered fields in such regions were time-stepped, and then added to a cancelling incident field to obtain the low total-field levels). Avoidance of subtraction noise is the key to obtaining near-field computational dynamic ranges exceeding 60 dB.

4) *Systematic computation of bistatic RCS.* The provision of a well-defined scattered-field region in the FD-TD lattice permits the near-to-far field transformation illustrated in Fig. 3b [13]. The dashed virtual surface shown in Fig. 3b can be located along convenient lattice planes in the scattered-field region of Fig. 3a. Tangential scattered E and H fields computed via FD-TD at this virtual surface can then be weighted by the free-space Green's function and integrated (summed) to provide the far-field response and RCS (full bistatic response for the assumed illumination angle) [13]-[15]. The near-field integration surface has a fixed rectangular shape independent of the shape or composition of the enclosed modeled structure.

d. Lattice Truncations

The fields at the outermost lattice planes cannot be computed using central differences because of the absence of known field data at points outside of the lattice. Therefore, an auxiliary lattice truncation condition is necessary. This condition must permit an outgoing scattered-wave numerical analog to exit the lattice without appreciable nonphysical reflection.

It has been shown that the required lattice truncation condition is really a radiation condition in the near field [16]-[18]. A successful second-order-accurate finite-difference approximation of the exact radiation condition in Cartesian coordinates was introduced in [12]. This was subsequently used in a variety of 2-D and 3-D FD-TD scattering codes [13]-[15], yielding excellent results for both near and far fields (including those of this paper). However, recent interest in improved models of scattering has prompted research in higher-order near-field radiation conditions [19]-[21]. The

goal is to reduce numerical noise due to imperfect lattice truncations by at least one order of magnitude (20 dB) relative to that achieved by [12].

4. CONTOUR PATH INTERPRETATION

The original FD-TD algorithm was devised to directly approximate the pointwise derivatives of Maxwell's time-dependent curl equations by numerical central differences [1]. While this thinking is useful for understanding how FD-TD models wave propagation in free space, it sheds little light on what modifications are needed to model the physics of fine structural features such as wires and slots requiring sub-cell spatial resolution.

Recent work has indicated that FD-TD modeling can be extended by starting with a more macroscopic description based upon Ampere's Law and Faraday's Law in *integral* form, implemented on an array of electrically small, spatially orthogonal contours. These contours mesh in the manner of links in a chain, filling the FD-TD modeled space. It can be easily shown that the original pointwise and new contour path interpretations are equivalent for the free-space case [22]. Further, it can shown that wires, slots, and curved surfaces can be modeled by incorporating appropriate field behavior into the contour and surface integrals implementing Ampere's Law and Faraday's Law at selected meshes, and by deforming contour paths as required to conform with surface curvature.

a. Example 1: Application to the Thin Slot

To illustrate how the contour path interpretation provides the basis for FD-TD modeling of fine geometrical features requiring sub-cell spatial resolution, we first consider the thin slot in a planar conducting screen (TE case) [22]. Fig. 4 illustrates the slot geometry and the Faraday's Law contour paths, C_1, C_2, and C_3, used to derive special FD-TD algorithms for the longitudinal magnetic field components, H_z, located immediately adjacent to the screen.

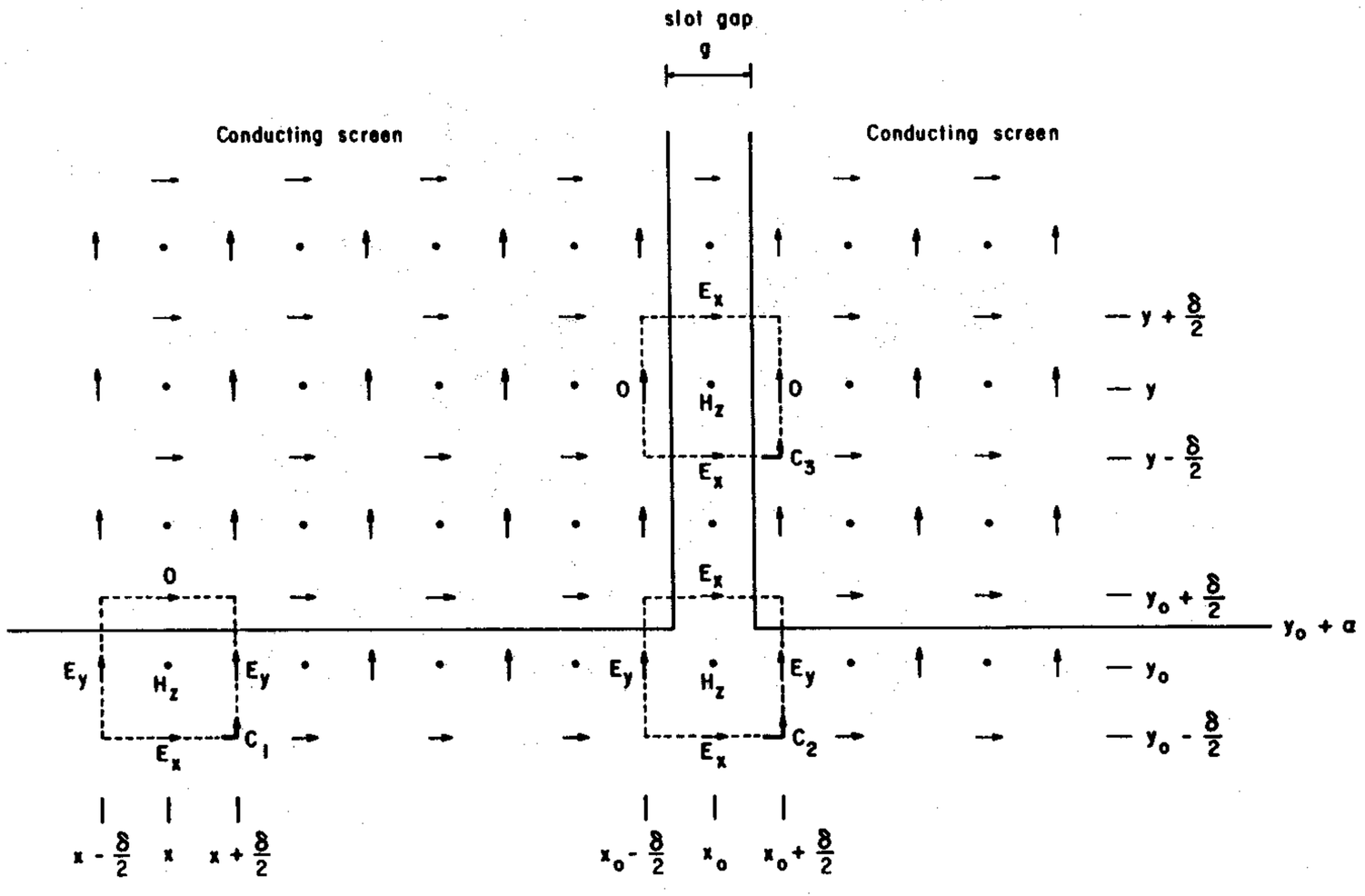

Fig. 4. Faraday's Law contour paths for the planar conducting screen with narrow straight slot (TE case).

Very simple assumptions are made regarding the field behavior near the slotted screen:

1) At contour C_1, H_z and E_y have no variation in y. Evaluated at the x midpoint of C_1, H_z and E_x represent the average values of their respective fields over the full x interval.

2) At contour C_2, H_z is the average value of the magnetic field over the free-space part of S_2. E_y has no variation in y, and E_x is the average value over the full x interval.

3) At contour C_3, H_z is the average value of the magnetic field over the full y interval, and H_z and E_x have no variation in the x direction (across the slot gap).

After applying Faraday's Law for the three contours subject to the above assumptions, the following special FD-TD time-stepping relations are obtained for H_z components [22]:

Away from the slot (contour C_1)

$$\frac{H_z^{n+\frac{1}{2}}(x,y_0)-H_z^{n-\frac{1}{2}}(x,y_0)}{\Delta t}\simeq \frac{[E_y^n(x-\frac{\delta}{2},y_0)-E_y^n(x+\frac{\delta}{2},y_0)]\cdot(\frac{\delta}{2}+\alpha)-E_x^n(x,y_0-\frac{\delta}{2})\cdot\delta}{\mu_0\delta(\frac{\delta}{2}+\alpha)} \tag{5a}$$

At the opening (aperture) of the slot (contour C_2)

$$\frac{H_z^{n+\frac{1}{2}}(x_0,y_0)-H_z^{n-\frac{1}{2}}(x_0,y_0)}{\Delta t}\simeq \frac{\begin{pmatrix} E_x^n(x_0,y_0+\frac{\delta}{2})\cdot g-E_x^n(x_0,y_0-\frac{\delta}{2})\cdot\delta+ \\ [E_y^n(x_0-\frac{\delta}{2},y_0)-E_y^n(x_0+\frac{\delta}{2},y_0)]\cdot(\frac{\delta}{2}+\alpha)\end{pmatrix}}{\mu_0\cdot[\delta(\frac{\delta}{2}+\alpha)+g(\frac{\delta}{2}-\alpha)]} \tag{5b}$$

Within the slot (contour C_3)

$$\frac{H_z^{n+\frac{1}{2}}(x_0,y)-H_z^{n-\frac{1}{2}}(x_0,y)}{\Delta t}\simeq \frac{E_x^n(x_0,y+\frac{\delta}{2})\cdot g-E_x^n(x_0,y-\frac{\delta}{2})\cdot g}{\mu_0 g\delta} \tag{5c}$$

No H or E components in the FD-TD grid other than these H_z components immediately adjacent to the screen require modified time-stepping relations.

b. Example 2: Application to the Thin Wire

The contour path interpretation is next applied to model coupling to a sub-cell diameter wire [23]. Fig. 5 illustrates the Faraday's Law contour path used to derive the special FD-TD algorithm for the circumferential H immediately adjacent to the wire.

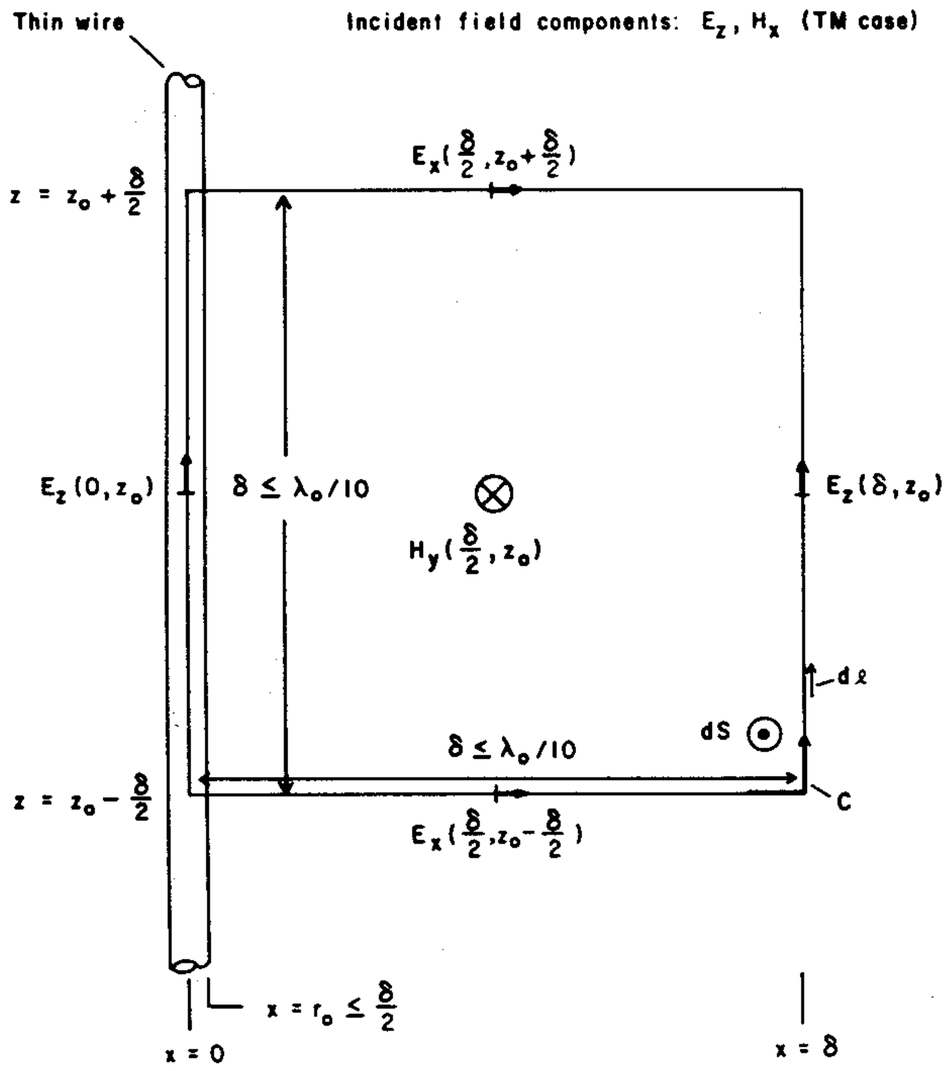

Fig. 5. Faraday's Law contour path for thin-wire model.

Although only H_y and E_x are shown, the analysis is easily generalized for the other adjacent looping H (H_x) and radial E (E_y). Very simple assumptions are made regarding the field behavior near the wire:

1) The *scattered* circumferential H and the *scattered* radial E components vary as 1/r, where r is the distance from the wire center. (In Fig. 5, 1/r is interpreted as 1/x.)

2) With r constrained to be less than $\lambda/10$ at any point in C by FD-TD spatial resolution requirements, the 1/r singularity behavior of the scattered circumferential H and radial E dominates the respective incident fields, so that the *total* circumferential H and *total* radial E also take on the 1/r singularity.

3) The total circumferential H and the total longitudinal E, evaluated at the z midpoint of the contour, represent the average values of their respective fields over the full z interval.

Using these assumptions, we now apply Faraday's Law along contour C. The 1/x varia-tions in H_y and E_x yield natural logarithms upon integration. This yields the following [23]:

$$\frac{H_y^{n+\frac{1}{2}}(\frac{\delta}{2}, z_0) - H_y^{n-\frac{1}{2}}(\frac{\delta}{2}, z_0)}{\Delta t} \simeq$$

$$\frac{[E_x^n(\frac{\delta}{2}, z_0 - \frac{\delta}{2}) - E_x^n(\frac{\delta}{2}, z_0 + \frac{\delta}{2})] \cdot \frac{1}{2} \ln\left(\frac{\delta}{r_0}\right) + E_z^n(\delta, z_0)}{\mu_0 \frac{\delta}{2} \ln\left(\frac{\delta}{r_0}\right)} \tag{6}$$

where r_0 (assumed to be less than $\delta/2$) is the wire radius. Isolation of $H_y^{n+1/2}(\delta/2, z_0)$ on the left hand side of (9) yields the required modified time-stepping relation. *No* H or E components in the FD-TD lattice other than the circumferential H components immediately adjacent to the wire require modified time-stepping relations.

c. Example 3: Application to Curved Surfaces

The contour path interpretation is last applied to model scattering by targets having curved surfaces [24]. Fig. 6 depicts the embedding of such a target in a 2-D TE grid. Faraday's Law can be used to define integration contours that either split or stretch selected grid cells in a manner to conform with the curved target surface. Very simple assumptions are made regarding the field behavior at these special cells:

1) Each H_z component is evaluated at its usual grid position, and is the average value within the patch bounded by the deformed cell contour.

2) Each E_x or E_y component is evaluated at its usual grid position, and is the average value over its respective straight portion of the cell contour.

3) Where possible, E_x and E_y are calculated by finite-differencing adjacent H_z's. Where such differencing would cut across the target surface, E_x or E_y is obtained *simply by taking the value* of its nearest co-linear E_x or E_y neighbor located on the same side of the target surface.

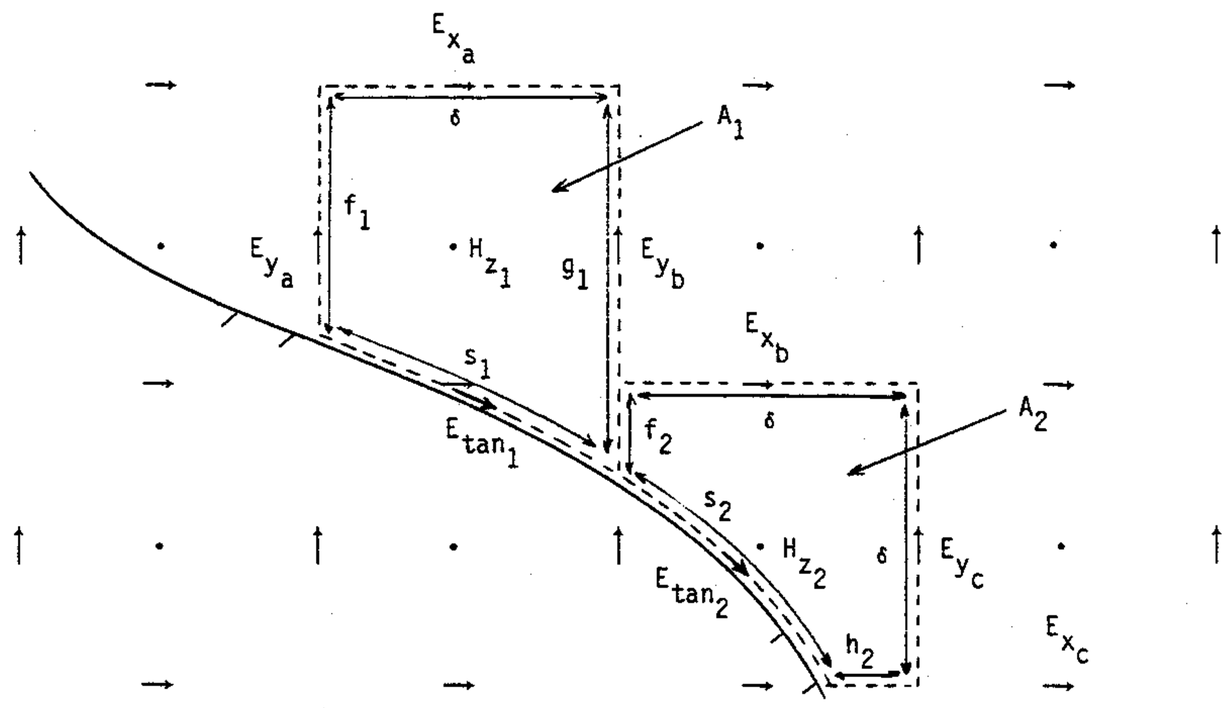

Fig. 6. Faraday's Law contour paths for conformal FD-TD modeling of a curved target.

4) An auxiliary field, E_{tan}, defined along the portion of the deformed cell contour that conforms to the target surface, represents the average value of the surface tangential E. For conducting targets having surface resistivity, E_{tan} can be easily related to the local tangential magnetic field by the surface resistivity, R_s.

5) For dielectric targets, E_{tan} is calculated by time-stepping using an Ampere's Law contour path that pierces the surface at a right angle. Exterior and interior H_z's needed for this time-stepping are obtained via linear interpolation of stored H_z's at standard grid locations.

Using these assumptions, we now apply Faraday's Law about the contours of Fig. 6 to obtain modified time-stepping relations for H_z suitable for conducting structures [24]:

Standard surface-conforming cell (contour C_1)

$$H_{z_1}^{n+\frac{1}{2}} \simeq C_1 \cdot H_{z_1}^{n-\frac{1}{2}} + D_1 \cdot [E_{y_a}^{n} \cdot f_1 - E_{y_b}^{n} \cdot g_1 + E_{x_a}^{n} \cdot \delta] \tag{7a}$$

where, assuming that R_{s1} is the local surface resistivity,

$$C_1 = \frac{(\frac{\mu_o A_1}{\Delta t} - \frac{s_1 R_{s_1}}{2})}{(\frac{\mu_o A_1}{\Delta t} + \frac{s_1 R_{s_1}}{2})} \quad ; \quad D_1 = \frac{1}{(\frac{\mu_o A_1}{\Delta t} + \frac{s_1 R_{s_1}}{2})} \tag{7b}$$

Non-standard surface-conforming cell (contour C_2)

$$H_{z_2}^{n+\frac{1}{2}} \simeq C_2 \cdot H_{z_2}^{n-\frac{1}{2}} + D_2 \cdot [E_{y_b}^{n} \cdot f_2 - E_{y_c}^{n} \cdot \delta + E_{x_b}^{n} \cdot \delta - E_{x_c}^{n} \cdot h_2] \tag{8a}$$

where, assuming that R_{s2} is the local surface resistivity,

$$C_2 = \frac{(\frac{\mu_o A_2}{\Delta t} - \frac{s_2 R_{s_2}}{2})}{(\frac{\mu_o A_2}{\Delta t} + \frac{s_2 R_{s_2}}{2})} \quad ; \quad D_2 = \frac{1}{(\frac{\mu_o A_2}{\Delta t} + \frac{s_2 R_{s_2}}{2})} \tag{8b}$$

This procedure allows the conformal modeling of arbitrary curved targets essentially as easily and as quickly as the original stepped-surface FD-TD code, but with substantially better accuracy. *No* H or E components in the FD-TD space grid other than the H_z components immediately adjacent to the object surface require modified time-stepping relations.

5. FD-TD MODELING VALIDATIONS FOR PENETRATION AND COUPLING

a. EM Wave Penetration Through a Narrow Slot

The accuracy of the contour path model for sub-cell-gap slots (Section 4a) will now be illustrated for the case of a straight slot in a thick conducting screen [22].

Fig. 7 depicts modeling results for a $\lambda/10$-thick conducting screen that extends $\lambda/2$ to each side of a straight slot which has a gap of $\lambda/40$. Broadside TE illumination is assumed. Three types of predictive data are compared: (a) A $\lambda/10$ FD-TD model using the contour path approach to treat the slot as a 1/4-cell gap; (b) A high-resolution ($\lambda/40$) FD-TD model treating the slot as a 1-cell gap; and (c) A very-high-resolution ($\lambda/400$ sampling in the slot) frequency-domain electric field integral equation (EFIE) model solved via MoM .

From Fig. 7, we see that there is excellent agreement between all three sets of predictive data in both magnitude and phase. It is seen that $\lambda/10$ FD-TD gridding can accurately model the physics of wave penetration through sub-cell slots with the contour path approach. This can substantially reduce computer resource requirements for FD-TD models of complex structures.

b. EM Wave Coupling to Thin Wires and Bundles

The accuracy of the contour path technique for modeling EM wave coupling to sub-cell-diameter wires (Section 4b) will now be illustrated for: (1) An infinitely long wire (over a wide range of radius); (2) A thin dipole; and (3) A wire-pair within a metal cavity [23].

Fig. 8a graphs the scattered azimuthal H field at a fixed distance of $\lambda/20$ from the center of an infinitely long wire having a radius ranging between $\lambda/30{,}000$ and $\lambda/30$.

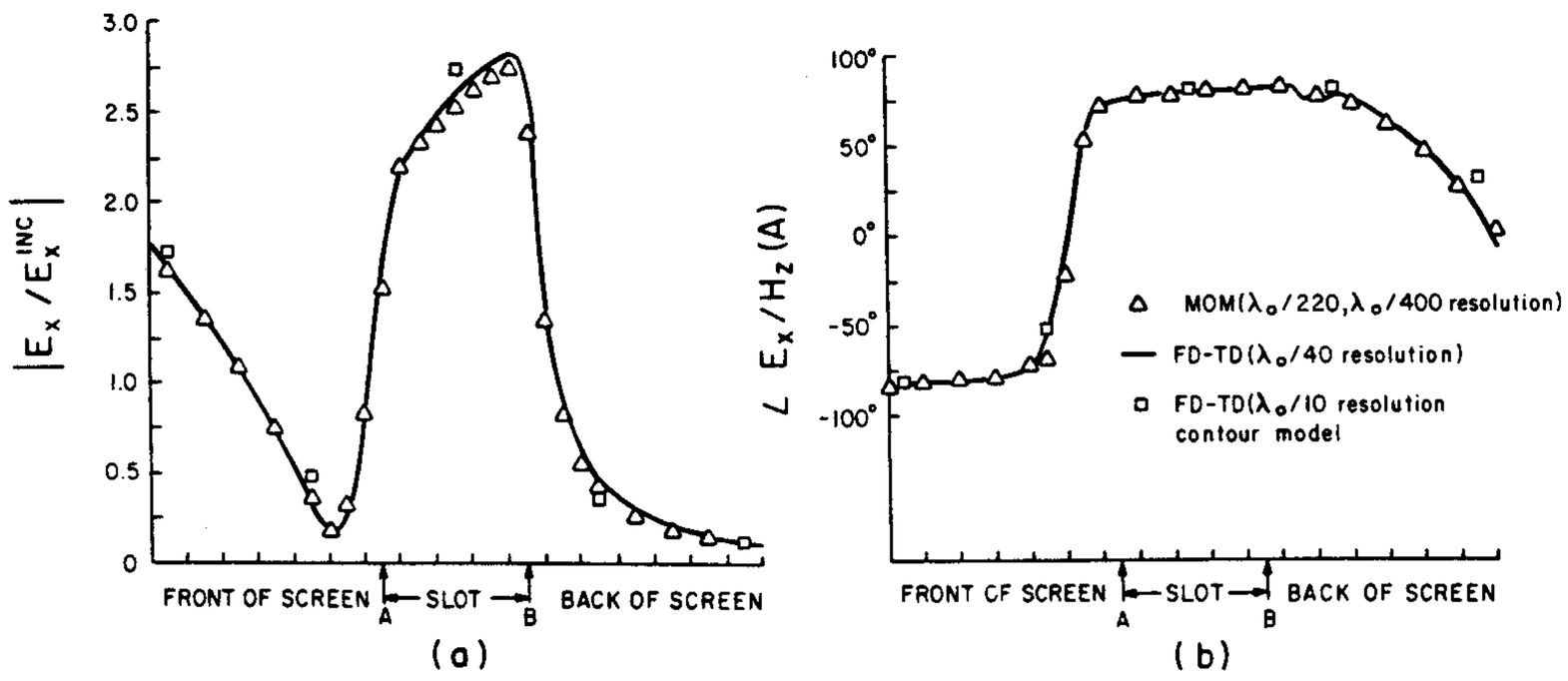

Fig. 7. Comparison of FD-TD and MoM solutions for the gap electric field distribution: (a) magnitude; (b) phase.

TM illumination is assumed. There is excellent agreement between the exact series solution and the $\lambda/10$ FD-TD contour path model over the entire 3-decade range of wire radius. Fig. 8b graphs the scattered azimuthal H distribution along a 2.0-λ (antiresonant) wire of radius $\lambda/300$. Broadside TM illumination is assumed, and the field is observed at a fixed distance of $\lambda/20$ from the wire center. There is excellent agreement between an EFIE MoM solution sampling the wire current at $\lambda/60$ increments and the $\lambda/10$ FD-TD contour path model.

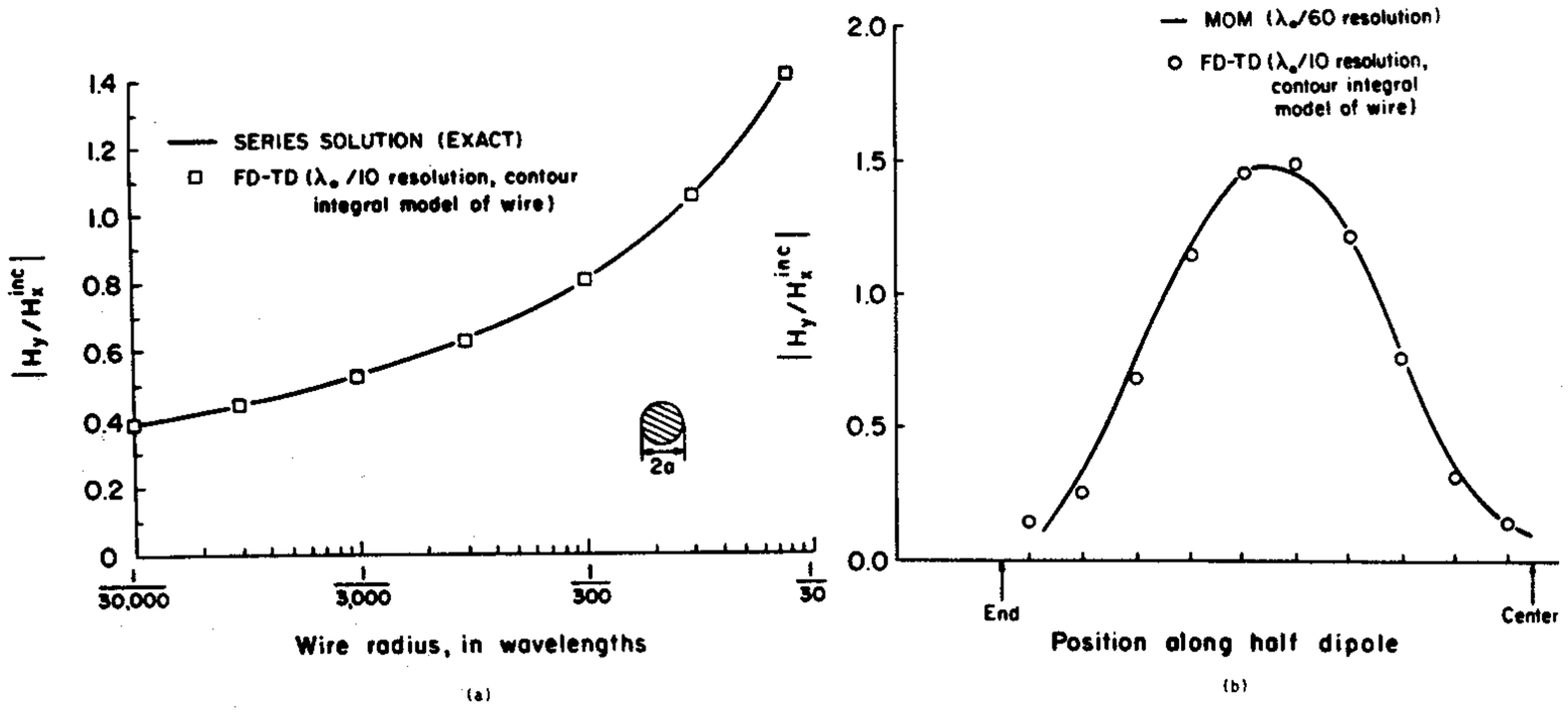

Fig. 8. Comparison of FD-TD and benchmark frequency-domain solutions for the scattered circumferential magnetic field: (a) infinite wire; (b) 2-λ wire.

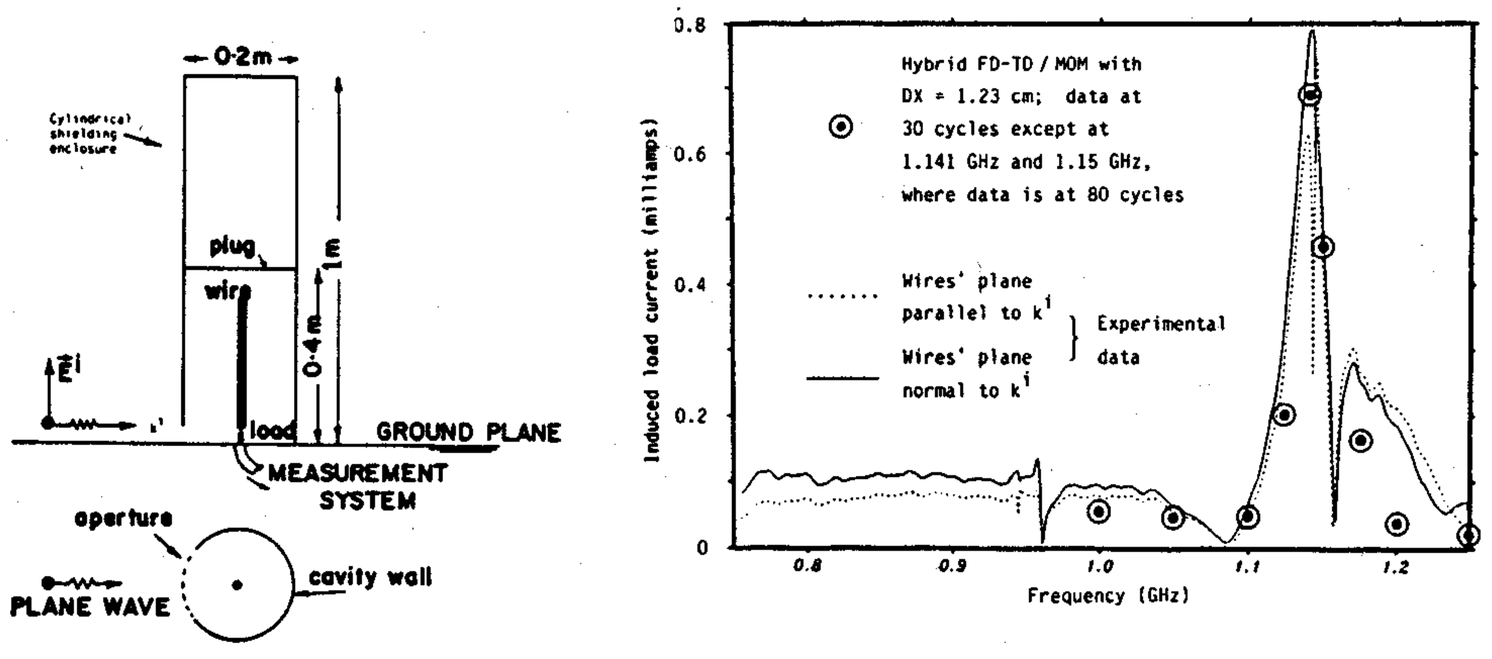

Fig. 9. Comparison of FD-TD and experimental data for coupling to a wire-pair in a cavity.

The FD-TD contour path model for single thin wires can be extended to treat thin wire bundles [23]. Fig. 9 shows the geometry and test results for such a model involving a wire-pair centered within a 3-D cylindrical metal cavity. The cavity, referenced to a large ground plane, is 1.0-m high, 20-cm diameter, and has an internal shorting plug located 40 cm above the ground plane. Approximate plane wave illumination in the band 0.75 - 1.25 GHz is provided by an electrically-large conical monopole. Wave penetration into the cavity is through a circumferential slot (12.5 cm arc length, 1.25 cm gap) at the ground plane. The internal pair is formed by two parallel wires (30-cm long, 0.495-mm radius) spaced 1 cm apart, with, respectively, 50-Ω and 0-Ω terminations to the ground plane.

From Fig. 9, we see that the predicted and measured wire load currents agree well. This test is challenging since the Q factor of the coupling response is quite high, about 75. Indeed, it is found that the FD-TD code has to be stepped through 80 cycles to approximately reach the sinusoidal steady state for illumination frequencies near the resonant peak [23].

6. FD-TD MODELING VALIDATIONS FOR SCATTERING AND RCS

Many analytical, code-to-code, and experimental validations have been obtained for FD-TD modeling of EM wave scattering and RCS. Selected validations will be reviewed here.

a. T-shaped Conducting Target, Multiple Monostatic Looks

We first consider the monostatic RCS pattern of a 3-D T-shaped conducting target [15] consisting of a 30 x 10 x 0.33 cm main plate and a 10 x10 x 0.33 cm bisecting fin (Fig. 10). The illumination is a 9.0-GHz plane wave at 0^o elevation angle and TE polarization relative to the main plate. Thus, the main plate spans 9.0λ and the fin 3.0λ. Note that look-angle azimuths between 90^o and 180^o exhibit the complicated physics of back-to-back corner reflectors.

For this target, the FD-TD model uses a uniform cell size of 0.3125 cm (λ/10.667), forming the main plate by 96 x 32 x 1 cells and the bisecting fin by 32 x 32 x 1 cells. The radiation boundary is located *only 8 cells* from the target, so that the lattice has 112 x 48 x 48 cells containing 1,548,288 unknown field components (212.6 λ^3). Starting with zero fields, 661 time steps are used (31 cycles of the incident wave).

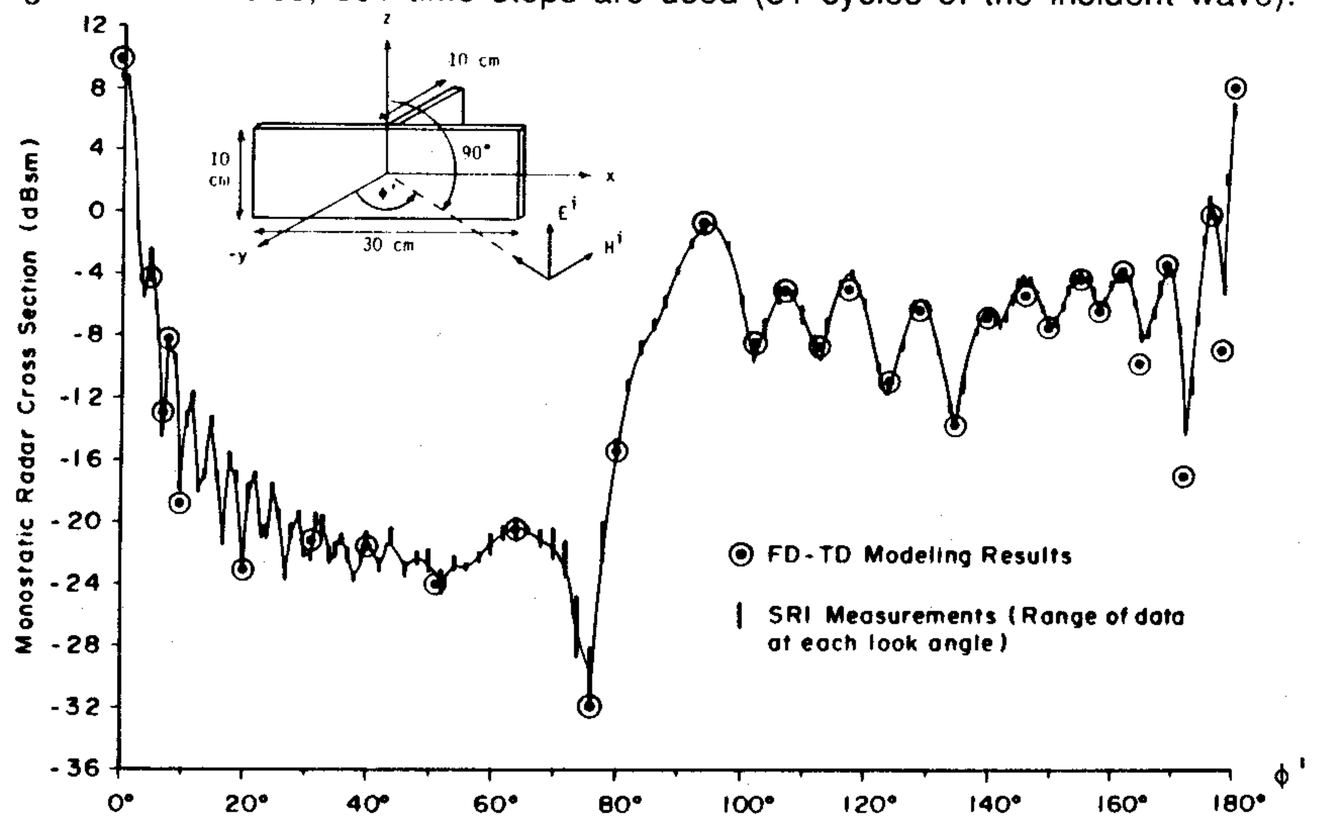

Fig. 10. Comparison of FD-TD and test data for monostatic RCS of the T-shaped target.

Fig. 10 compares the FD-TD predicted monostatic RCS values to measured data at 32 key look angles that define the major peaks and nulls of the pattern. The agreement is excellent: in amplitude, within 1 dB over a 40-dB dynamic range; and in azimuth, within 1^{o}. Computer running time is about 12 seconds per monostatic angle on the Cray Y-MP.

b. Trihedral Corner Reflector, Both Bare Metal and RAM Coated

We next consider the monostatic RCS pattern of a 3-D conducting trihedral corner reflector, both uncoated and with commercial RAM coating. The reflector consists of three, thin, 15 x 15 cm flat plates mounted at mutual 90^{o} angles (Fig. 11a). The illumination is a 10-GHz plane wave at 45^{o} azimuth angle and θ-directed E-field. Thus, the reflector spans 5 x 5 x 5 λ. For the coated case, the RAM is assumed to be Emerson & Cuming Type AN-73 (0.9525 cm thick, consisting of 3 distinct lossy layers of equal thickness).

For this target, the FD-TD cell size is 0.25 cm ($\lambda/12$), with each plate spanned by 60 x 60 cells. The radiation boundary is located *only 12 cells* from the target, so that the lattice has 84 x 84 x 84 cells containing 3,556,224 unknown field components (343 λ^3). Starting with zero fields, 720 time steps are used (30 cycles of the incident wave).

Fig. 11b compares the FD-TD computed monostatic RCS pattern in the θ plane (ϕ fixed at 45^{o}) with predictions made by the shooting and bouncing ray (SBR) code developed by S. W. Lee of the University of Illinois at Urbana. Excellent agreement is seen for the uncoated target case. For the RAM-coated case, both codes predict substantial reduction of the RCS response. It is seen that the predicted RCS patterns for this case are in good qualitative agreement. Computer running time is about 30 seconds per monostatic angle on the Cray Y-MP.

c. Wing-Like Target, Conformally Modeled

To help evaluate the accuracy of the conformal curved surface model (Section 4c) for monostatic RCS, we last consider a conducting wing-like target. The target, shown in

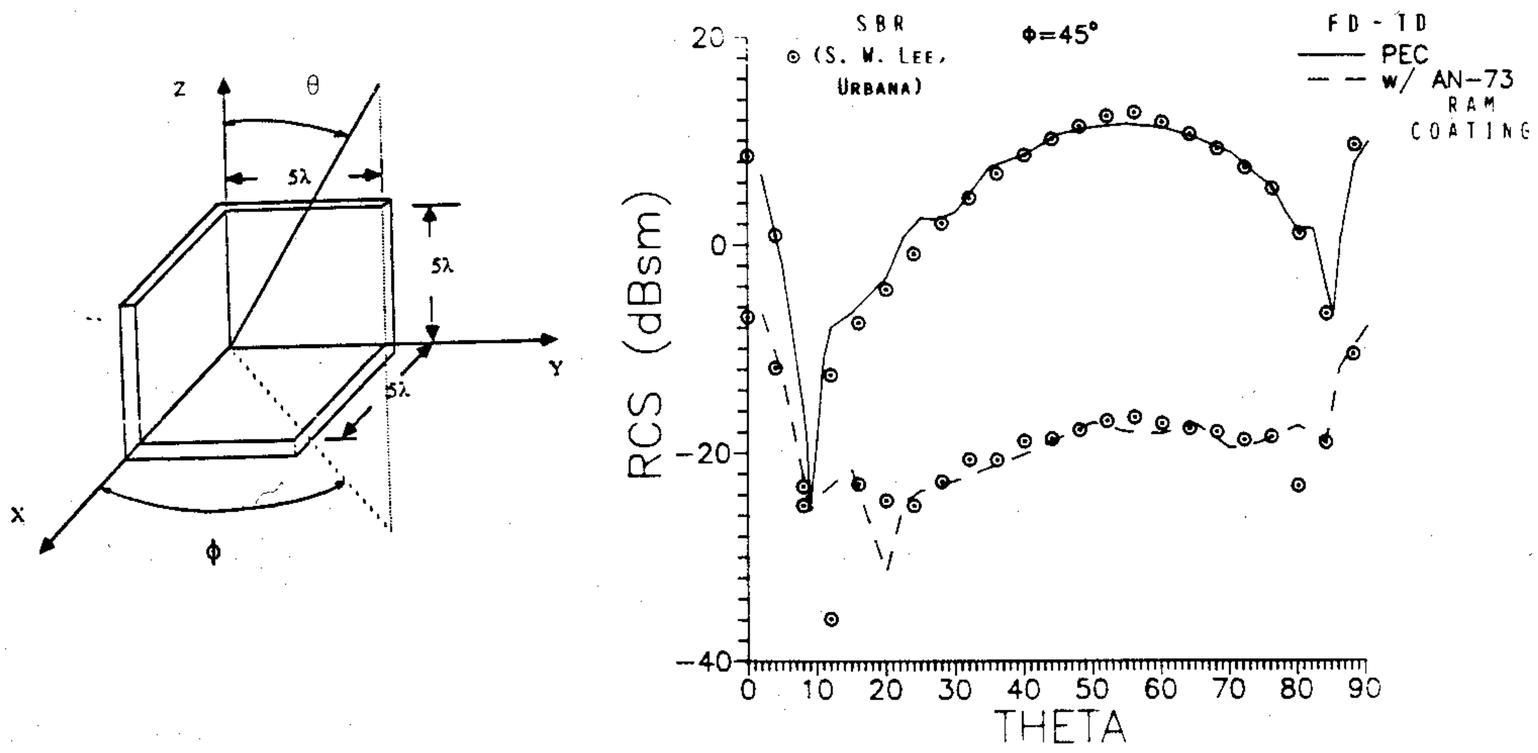

Fig. 11. FD-TD vs. SBR data for monostatic RCS of a trihedral corner reflector.

Fig 12, consists of a 10" by 12" metal plate, flat on one side and having steeply sloped sides with a central 6"-radius chamfer on the other. The plane-wave illumination is at 10 GHz with the incident-wave electric field polarized vertically (parallel to the 12" edge). Viewing the 12" edge of the plate as the z axis, $\theta^{inc} = 90^o$, and the monostatic RCS pattern is obtained as the azimuth angle is varied from -90^o (broadside to the flat side of the target) to $+90^o$ (broadside to the chamfer).

To permit direct code-to-code validation of FD-TD versus an existing, well-characterized 2-D MoM program, it was decided that all numerical modeling runs should be in 2-D (effectively letting the 12" dimension of the plate go to infinity). This allows acceptable MoM matrix size at 10 GHz, where the 10" side of the target spans 8.47λ. In addition, *both* the FD-TD and MoM predictions were compared to anechoic chamber measurements (although, of course, these data were obtained for the original 3-D target, not the 2-D idealizations).

Fig. 12 graphs comparative MoM, FD-TD, and measured monostatic RCS data for the wing-like target. The FD-TD and MoM data virtually overlay each other for observation angles between $+60^o$ and $+90^o$, where the chamfer is being directly illuminated and conformal target surface modeling is essential to obtain the proper RCS. Excellent agreement is also noted for observation angles between -90^o and -30^o, where the flat side is being directly illuminated. There is some disagreement of the predictive and measured data at grazing. However, the disagreement at these relatively low RCS levels is likely a consequence of the idealized 2-D models versus the 3-D physics actually being measured in the anechoic chamber.

d. Jet Engine Inlet, Conformally Modeled

To illustrate the emerging potential of FD-TD to achieve 3-D conformal models of electrically large structures, we last consider a curved jet engine inlet illuminated by a plane wave at 10 GHz. The inlet is assumed to be embedded within a conducting box coated with Type AN-73 RAM (see Example 6b above) to eliminate wave reflections from the outside of its curved sidewalls. With the box dimensions set at 30" x 10.5" x 10", the overall inlet/box target configuration spans 25.4λ x 8.89λ x 8.47λ. For this target, the

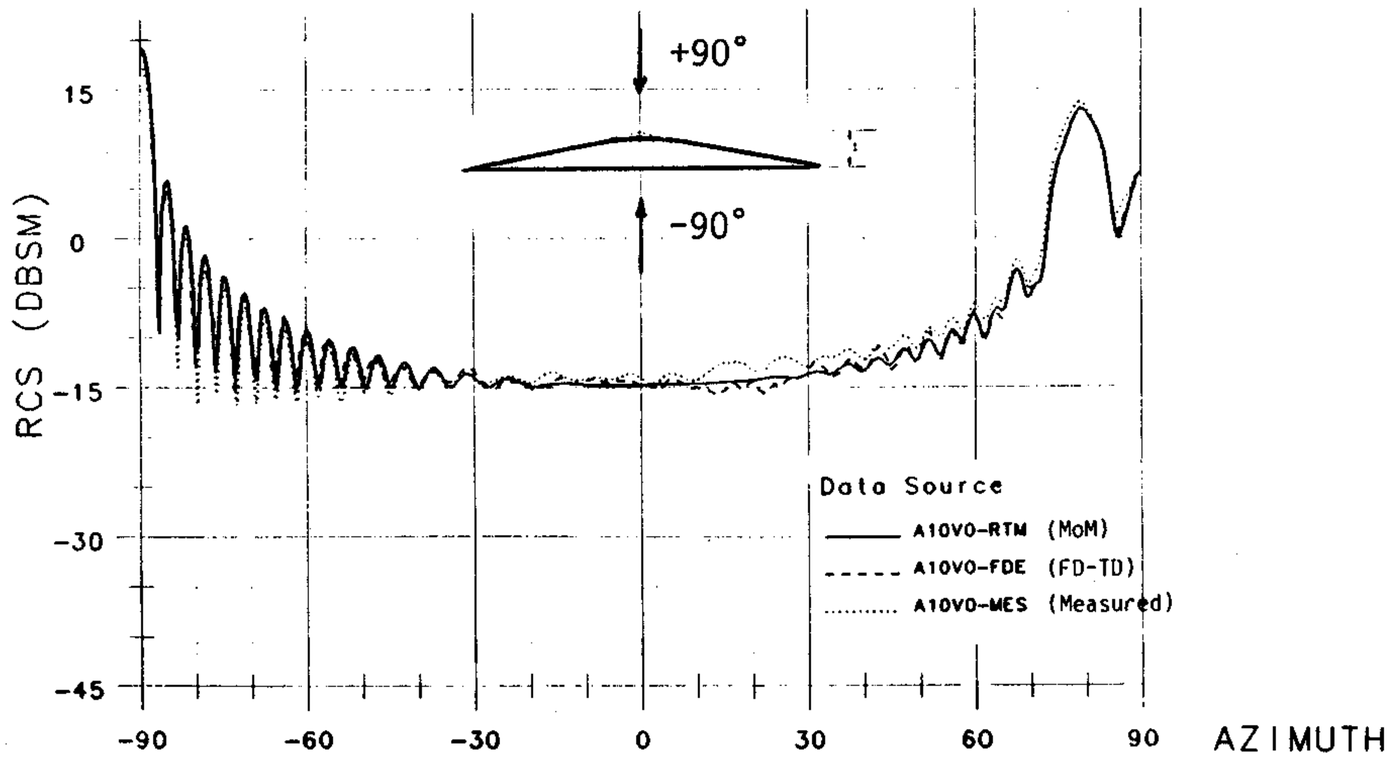

Fig. 12. Comparison of FD-TD, MoM, and measured RCS data for the wing-like target.

FD-TD cell size is 1/8" (λ/9.43), and the overall lattice has 270 x 122 x 118 cells containing 23,321,520 unknown field components (4,608 λ^3). Starting with zero-field initial conditions, 1800 time steps are used (95.25 cycles of the incident wave). Computer running time is about 8 minutes per monostatic angle on the Cray Y-MP.

Fig. 13 depicts the instantaneous distribution of the total electric field in a 2-D observation plane cutting through the center of the 3-D engine inlet. (This black and white photograph is derived from a color videotape display of the propagating electric field penetrating the inlet, generated directly by the FD-TD time-stepping.) The display is taken late in the time-stepping when the internal field is settled into a repetitive sinusoidal oscillation (standing wave). Light and dark bands indicate the positive and negative values of the field at one point in time of the standing wave. The incident wave is assumed to propagate from right to left, and is polarized so that its electric field points across the narrow dimension of the inlet. The aperture of the inlet is located at the right, and the inlet is shorted by a conducting wall representing the turbine assembly at the far left.

Clearly, in addition to simple data for the RCS pattern, FD-TD modeling provides details of the complex standing wave pattern within the engine inlet, especially when visualized in the time domain using color video technology. The latter visualization shows that a general pulsing of the field pattern within the inlet occurs in the sinusoidal steady state, emitting backscattered energy in a regular series of bursts. It may be possible to use this highly detailed time-domain near-field information to better design such articles in the future.

We note, in comparison, that if the frequency-domain MoM were applied to this engine inlet, a linear system involving approximately 450,000 equations in 450,000 unknowns would have to be set up and solved. This assumes the standard triangular surface patching implementation of the electric field integral equation, with the 1500 λ^2 area of the engine inlet discretized at 10 divisions per λ. Using an optimized out-of-memory subroutine for LU decomposition developed by Cray Research, the Cray Y-MP running time for this matrix would be about 2.6 years, with the Y-MP running essentially at top speed (2.1 Gflops). This compares to about *8 minutes* per monostatic observation angle for FD-TD, equivalent to 28 days for 5000 monostatic angles. Additional problems involved in error accumulation in the LU decomposition and reliability of the computer system over the multi-year solution time probably would combine to render a traditional MoM solution useless for this target and those of similar or larger electrical sizes. We note also that the MoM solution does not directly provide details of the penetrating near-field distribution.

7. PRESENT STATUS AND FUTURE DIRECTIONS OF FD-TD

At present, 3-D FD-TD conformal models of electrically large structures spanning more than 30λ are being developed. These are apparently the largest detailed computational EM models ever attempted. Unresolved issues at this time include: (1) Automated FD-TD lattice generation for conformal modeling in 3-D; (2) Development of sub-cell models for thin-layer coatings of structure surfaces; (3) Understanding the accuracy limitations caused by numerical artifacts (such as lattice modal phase velocity dispersion and imperfect radiation boundary conditions) at this unprecedented modeling scale; (4) Understanding the time-domain convergence properties of electrically-large 3-D structures, especially those having reentrant or cavity-like features; (5) Efficiently incorporating the dispersive nature of material electrical properties in the time-marching algorithm; and (6) Developing highly efficient multi-processing software for computer types represented by the Cray 3, Cray Y-MP, and Thinking Machines CM-2 (on the latter two machines, especially for large "out-of-memory" problems).

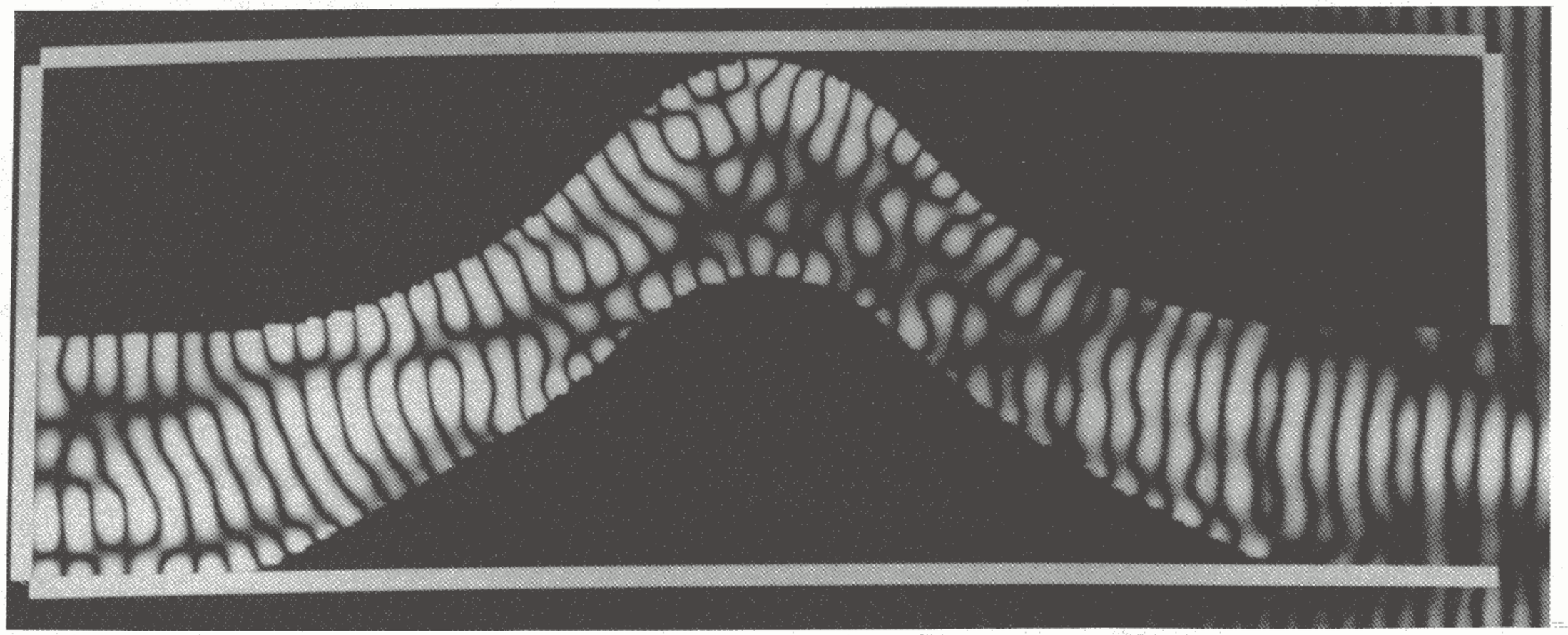

Fig. 13. FD-TD computed instantaneous distribution of the total electric field in a 2-D observation plane cutting through the center of the 3-D engine inlet.

By 1995, it is almost certain that 10-Gflop computers having 10 Gwords of fast memory will be routinely available to the academic and engineering communities. These would permit in-memory 3-D FD-TD models of structures spanning $100-300\ \lambda$ (depending upon the precise shape) to be run. At 10 GHz, this would imply 3-D structure sizes of 3 - 10 m (up to 30 feet in span) to be modeled with a uniform spatial resolution of 3 mm (1/8 inch). Advanced out-of-memory FD-TD software should enable even larger structures to be modeled in their entirety with uniformly fine spatial resolution. Thus, for microwave frequencies up to about 10 GHz, the era of the "entire airplane in the grid" would be opened. Automated FD-TD geometry generation would permit the EM modeling to utilize structure databases developed by non-EM engineers, leading to design cost reduction and the possibility of innovative design optimizations.

8. CONCLUSION

This paper has reviewed the basic formulation of the FD-TD numerical modeling approach for Maxwell's equations. A number of examples of FD-TD modeling of electromagnetic wave interactions with structures were provided to indicate the accuracy and breadth of FD-TD applications. In all cases studied to date where rigorous analytical, code-to-code, or experimental validations were possible, FD-TD predictive data for penetrating and scattered near fields as well as RCS are in excellent agreement with benchmark data. With continuing advances in FD-TD modeling theory and continuing advances in supercomputer technology, it is likely that FD-TD numerical modeling will occupy an important place in high-frequency engineering electromagnetics in the 1990's.

ACKNOWLEDGEMENTS

The authors wish to acknowledge the support of National Science Foundation Grant ASC-8811273; Office of Naval Research Contract N00014-88-K-0475; General Dynamics PO-4059045; Cray Research Inc.; and the National Center for Supercomputing Applications.

REFERENCES

[1] Yee, K. S., ``Numerical solution of initial boundary value problems involving Maxwell's equations in isotropic media," *IEEE Trans. Antennas Propagat.*, **AP-14**, 302-307, May 1966.

[2] Taflove, A., and M. E. Brodwin. ``Numerical solution of steady-state electromagnetic scattering problems using the time-dependent Maxwell's equations," *IEEE Trans. Microwave Theory Tech.*, **MTT-23**, 623-630, August 1975.

[3] Kriegsmann, G. A., ``Exploiting the limiting amplitude principle to numerically solve scattering problems," *Wave Motion*, **4**, 371-380, 1982.

[4] Taflove, A., and M. E. Brodwin. ``Computation of the electromagnetic fields and induced temperatures within a model of the microwave-irradiated human eye," *IEEE Trans. Microwave Theory Tech.*, **MTT-23**, 888-896, Nov. 1975.

[5] D. T. Borup, D. M. Sullivan, and O. P. Gandhi, "Comparison of the FFT conjugate gradient method and the finite-difference time-domain method for the 2-D absorption problem," *IEEE Trans. Microwave Theory Tech.*, **MTT-35**, 383-395, April 1987.

[6] Taflove, A., ``Application of the finite-difference time-domain method to sinusoidal steady state electromagnetic penetration problems," *IEEE Trans. Electromagn. Compat.*, **EMC-22**, 191-202, Aug.1980.

[7] Taflove, A., and K. R. Umashankar, ``A hybrid moment method/finite-difference time-domain approach to electromagnetic coupling and aperture penetration into complex geometries," *IEEE Trans. Antennas Propagat.*, **AP-30**, 617-627, July 1982.

[8] Taflove, A., and K. R. Umashankar, ``Advanced numerical modeling of microwave penetration and coupling for complex structures," Final Rept. No. UCRL-15960, Contract 6599805, Lawrence Livermore Nat. Lab., 1987.
[9] Holland, R., ``Threde: A free-field EMP coupling and scattering code," *IEEE Trans. Nuclear Sci.*, **NS-24**, 2416-2421, Dec. 1977.
[10] Kunz, K. S., and K. M. Lee, ``A three-dimensional finite-difference solution of the external response of an aircraft to a complex transient EM environment: Part I, The method and its implementation," *IEEE Trans. Electromagn. Compat.*, **EMC-20**, 328-333, May 1978.
[11] Merewether, D. E., R. Fisher, and F. W. Smith, ``On implementing a numeric Huygens' source scheme in a finite-difference program to illuminate scattering bodies," *IEEE Trans. Nuclear Sci.*, **NS-27**, 1819-1833, Dec. 1980.
[12] Mur, G., ``Absorbing boundary conditions for the finite-difference approximation of the time-domain electromagnetic field equations," *IEEE Trans. Electromagn. Compat.*, **EMC-23**, 377-382, Nov. 1981.
[13] Umashankar, K. R., and A. Taflove, ``A novel method to analyze electromagnetic scattering of complex objects," *IEEE Trans. Electromagn. Compat.*, **EMC-24**, 397-405, Nov. 1982.
[14] Taflove, A., and K. R. Umashankar, ``Radar cross section of general three-dimensional scatterers," *IEEE Trans. Electromagn. Compat.*, **EMC-25**, 433-440, Nov. 1983.
[15] Taflove, A., K. R. Umashankar, and T. G. Jurgens, ``Validation of FD-TD modeling of the radar cross section of three-dimensional structures spanning up to nine wavelengths," *IEEE Trans. Antennas Propagat.*, **AP-33**, 662-666, June 1985.
[16] Engquist, B., and A. Majda, ``Absorbing boundary conditions for the numerical simulation of waves," *Math. Comp.*, **31**, 629-651, July 1977.
[17] Trefethen, L. N., and L. Halpern, ``Well-posedness of one-way wave equations and absorbing boundary conditions," Inst. Comput. Appl. Sci. and Engrg. (ICASE), NASA Langley Res. Ctr., Hampton, VA, Rept. 85-30, 1985.
[18] Bayliss, A., and E. Turkel, "Radiation boundary conditions for wave-like equations," *Commun. Pure. Appl. Math.*, **33**, 707-725, 1980.
[19] Moore, T. G., J. G. Blaschak, A. Taflove, and G. A. Kriegsmann, ``Theory and application of radiation boundary operators," *IEEE Trans. Antennas Propagat.*, **36**, 1797-1812, Dec. 1988.
[20] Blaschak, J. G., and G. A. Kriegsmann, ``A comparative study of absorbing boundary conditions," *J. Computational Physics*, **77**, 109-139, July 1988.
[21] J. Fang and K. K. Mei, "A super-absorbing boundary algorithm for solving electromagnetic problems by time-domain finite-difference method," in *Proc. 1 988 IEEE AP-S Int. Symp.* (Syracuse, NY, June 1988), 472-475.
[22] Taflove, A., K. R. Umashankar, B. Beker, F. Harfoush, and K. S. Yee, ``Detailed FD-TD analysis of electromagnetic fields penetrating narrow slots and lapped joints in thick conducting screens," *IEEE Trans. Antennas Propagat.*, **AP-36**, 247-257, Feb. 1988.
[23] Umashankar, K. R., A. Taflove, and B. Beker, ``Calculation and experimental validation of induced currents on coupled wires in an arbitrary shaped cavity," *IEEE Trans. Antennas Propagat.*, **AP-35**, 1248-1257, Nov. 1987.
[24] Jurgens, T. G., A. Taflove, T. G. Moore, and K. R. Umashankar, ``FD-TD conformal modeling of curved surfaces," submitted to *IEEE Trans. Antennas Propagat.*